Imaging uncompensated moments and exchange-biased emergent ferromagnetism in FeRh thin films

Isaiah Gray, Gregory M. Stiehl, John T. Heron, Antonio B. Mei, Darrell G. Schlom, Ramamoorthy Ramesh, Daniel C. Ralph, and Gregory D. Fuchs

Phys. Rev. Materials **3**, 124407 — Published 19 December 2019

DOI: 10.1103/PhysRevMaterials.3.124407

Imaging uncompensated moments and exchange-biased emergent ferromagnetism in FeRh thin films

Isaiah Gray,[1,2] Gregory M. Stiehl,[3] John T. Heron,[4] Antonio B. Mei,[5] Darrell G. Schlom,[5] Ramamoorthy Ramesh,[6,2] Daniel C. Ralph,[3,2] and Gregory D. Fuchs[1,2]

[1]*School of Applied and Engineering Physics, Cornell University, Ithaca, NY, 14853, USA*

[2]*Kavli Institute at Cornell, Cornell University, Ithaca, NY, 14853, USA*

[3]*Department of Physics, Cornell University, Ithaca, NY, 14853, USA*

[4]*Department of Materials Science and Engineering, University of Michigan, Ann Arbor, Ann Arbor, Michigan, 48109, USA*

[5]*Department of Materials Science and Engineering, Cornell University, Ithaca, NY, 14853, USA*

[6]*Department of Materials Science and Engineering, University of California, Berkeley, CA, 94720, USA*

(Dated: September 20, 2019)

Abstract

Uncompensated moments in antiferromagnets are responsible for exchange bias in antiferromagnet/ferromagnet heterostructures; however, they are difficult to directly detect because any signal they contribute is typically overwhelmed by the ferromagnetic layer. We use magneto-thermal microscopy to image micron-scale uncompensated moments in thin films of FeRh, a room-temperature antiferromagnet that exhibits a 1st-order phase transition to a ferromagnetic state near 400 K. FeRh provides the unique opportunity to study both uncompensated moments in the antiferromagnetic phase and the interaction of uncompensated moments with emergent ferromagnetism within a relatively broad (390 K - 420 K) temperature range near T_C. In the AF phase below T_C, we image both pinned UMs, which cause local vertical exchange bias, and unpinned UMs, which exhibit an enhanced coercive field that reflects exchange-coupling to the AF bulk. Near T_C, where AF and FM order coexist, we find that the emergent FM order is exchange-coupled to the bulk Néel order. This exchange coupling leads to the nucleation of unusual configurations in which FM domains are pinned in different in-plane orientations, even in the presence of a nominally saturating magnetic field, before suddenly collapsing into a state uniformly parallel to the field.

I. INTRODUCTION

In an ideal Néel antiferromagnet, each lattice-site spin is adjacent to an oppositely-pointing spin such that all spins are compensated[1]. In real antiferromagnets, crystal defects[2], strain[3], and surface roughness[4] (among other mechanisms) cause some spins to be uncompensated, resulting in local magnetic moments within the antiferromagnet[5,6].

Far from being a mere material imperfection, these uncompensated moments (UMs)[7] are responsible for exchange bias in antiferromagnet (AF)/ferromagnet (FM) heterostructures[8,9], the most important current application of antiferromagnets due to its crucial role in pinning the FM layer in magnetoresistive sensors and other devices[10]. The exchange interaction between the AF and FM layers acts as an effective magnetic field which shifts the $M(H)$ loop of the FM along the horizontal field axis[11], producing exchange bias (EB). The underlying mechanisms of exchange bias are complex: The interfacial FM spins are not coupled to the entire AF surface as initially thought[12] but instead to uncompensated spins which comprise a small percentage of the AF surface[13,14].

In addition to the interfacial AF spins that directly exchange-couple to the FM spins, UMs from uncompensated spins in the bulk also contribute to exchange bias. For example, experimentally altering the bulk AF domain structure by introducing bulk defects via irradiation[2] affects the magnitude of EB, even if the AF/FM interface is unchanged. According to the domain state model[15] of exchange bias, bulk AF domains acquire net magnetization upon field-cooling from above the Néel temperature T_N – both at domain walls and within the domains themselves – and the resulting bulk UMs stabilize interfacial UMs[9].

Despite their critical role in exchange bias, bulk UMs are difficult to study directly. Any signal bulk UMs produce is typically overwhelmed by the FM layer in bulk magnetization measurements[16]. Although imaging techniques such as magnetic force microscopy[17] and XMCD-PEEM[18] can successfully probe UMs, these techniques are primarily surface-sensitive. Therefore, a detailed experimental understanding of how the spatial structure of the bulk UMs stabilizes the interfacial UMs is still lacking[9].

The metallic AF FeRh offers a potential path to circumvent the difficulties of directly studying UMs. An antiferromagnet at room temperature, it undergoes an unusual 1st-order phase transition from AF to FM near 400 K[19]. This transition is interesting in itself – the exact mechanism is still debated[20] – and is also exploited in potential electric field-

assisted[21–23] and heat-assisted[24] magnetic recording devices. Within the relatively broad transition region – between 20 K and 30 K wide depending on the composition – AF and FM phases coexist and interact. The phase transition allows detection of UMs in the AF phase, where they are not overwhelmed by FM moments, and then study of the interaction between UMs and emergent ferromagnetism within the transition region.

In this work we image micron-scale uncompensated moments and emergent FM in FeRh using magneto-thermal microscopy[25–31], which is based on through-plane thermal gradients within the AF thin film and therefore can potentially probe bulk UMs. Below the transition temperature T_C, we resolve pinned and unpinned UMs within the AF film, which result in *vertical* exchange bias that locally shifts the entire $M(H)$ loop above or below zero. Near T_C, we find that the emergent FM phase is exchange-coupled to the bulk AF order. Our images reveal a disordered exchange-biased AF/FM system in which FM domains are pinned in different in-plane directions, even when the applied magnetic field is much greater than the coercive field in the FM phase. These results demonstrate previously unobserved exchange bias within a metamagnetic phase transition and suggest a general method for spatially resolving uncompensated moments in AF metals with magneto-thermal microscopy.

II. IMAGING UNCOMPENSATED MOMENTS IN FeRh IN THE AF PHASE

A. Experimental setup and materials

Magneto-thermal microscopy is based on the anomalous Nernst effect (ANE)[26,28,29] and the longitudinal spin Seebeck effect (LSSE)[27,30]. In the anomalous Nernst effect, a thermal gradient $\boldsymbol{\nabla} T$ in a magnetic conductor with moment $\boldsymbol{m}$ produces an electric field $\boldsymbol{E} = -N\mu_0 \boldsymbol{\nabla} T \times \boldsymbol{m}$. In the longitudinal spin Seebeck effect, a thermal gradient $\boldsymbol{\nabla} T$ within a magnetic material generates a pure spin current $\boldsymbol{j}_s \parallel \boldsymbol{\nabla} T$. If the magnetic material is interfaced with a heavy metal, some of $\boldsymbol{j}_s$ diffuses into the heavy metal where it is transduced by the inverse spin Hall effect into a charge current $\boldsymbol{j}_c \perp \boldsymbol{j}_s$. Because ANE and LSSE have the same symmetry, in both cases an out-of-plane $\boldsymbol{\nabla} T$ produces a local $\boldsymbol{E}$ proportional to the in-plane magnetic moment.

We generate local thermal gradients with a focused pulsed Ti:Sapphire laser using an experimental setup detailed in our previous work[26–30]. We employ 3 ps-wide pulses at 785

nm wavelength, focused to a 650 nm-diameter spot using an optical microscope objective. In a patterned device, the electric field $\boldsymbol{E}$ generates a voltage drop between the device contacts that depends only on $\boldsymbol{\nabla} T$ and $\boldsymbol{m}$ within the excited region. Therefore, by raster scanning the laser over the device and reading the resulting V_{ANE} voltage pulses, we build up a spatial map of the in-plane moment. We collect the V_{ANE} pulses into a microwave transmission line before amplifying and measuring them using a homodyne technique as described in our previous work[26]. All images in the main text are taken at 3 mJ/cm^2 laser fluence.

We image epitaxial MgO(001)/20 nm FeRh(001)/8 nm Pt, patterned into 3 μm $\times$ 18 μm Hall crosses by photolithography and ion milling. The FeRh is sputtered from a stoichiometric $Fe_{0.49}Rh_{0.51}$ target; from x-ray diffraction data in Appendix A and Vegard's law, we estimate the composition of the film to be $Fe_{0.47}Rh_{0.53}$. The Pt is sputtered primarily as a capping layer to protect the FeRh from oxidizing, and additionally to enable the possibility of signal from LSSE as well as ANE. Additional magneto-thermal images of uncapped 35 nm-thick MgO(001)/$Fe_{0.52}Rh_{0.48}$ and MgO(001)/$Fe_{0.43}Rh_{0.57}$ shown in Appendix D yield similar signal magnitudes as the 20 nm-thick $Fe_{0.47}Rh_{0.53}$/Pt, which indicates that a potential LSSE signal is smaller than the signal contribution from ANE[32]. Therefore the Pt layer does not affect our conclusions, and for convenience we refer to ANE plus a potential smaller FM LSSE as ANE.

B. Pinned and unpinned uncompensated moments at 300 K

We first image FeRh/Pt at room temperature, in the AF phase, as a function of applied magnetic field H_{app}. Fig. 1 shows ANE images of a 3 μm cross at $H_{app} = \pm 2.4$ kOe along the x-direction. To probe both x and y-components of the magnetization, we make contact to the Hall cross in an L-shape, illustrated in Fig. 1(a). V_{ANE} is proportional to the in-plane component of $\boldsymbol{m}$ locally perpendicular to the device channel. Therefore, in the vertical branch we measure m_x such that blue and orange contrast represents spins pointing right and left, respectively. In the horizontal branch we measure m_y and blue such that orange contrast represents spins pointing up and down, respectively.

In the vertical branch in Fig. 1(b) we observe micron-scale regions of positive and negative contrast which partially switch with field. Unlike anomalous Nernst images of ferromagnets[26,28,29], V_{ANE} does not uniformly saturate with the field, which indicates that

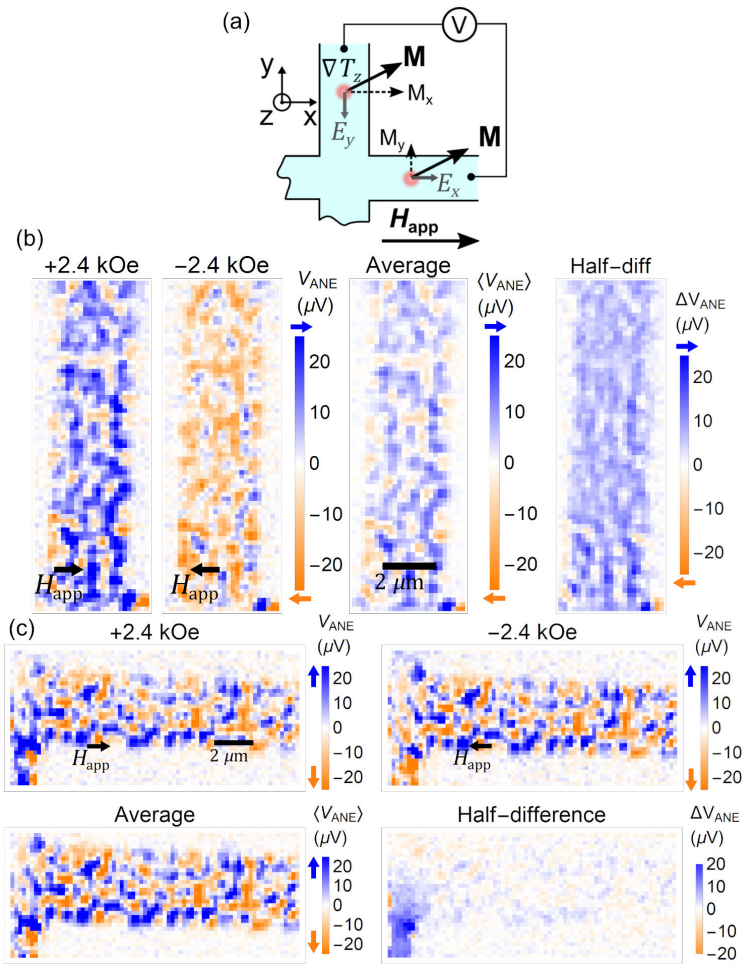

FIG. 1: Anomalous Nernst imaging of MgO(001)/20 nm $Fe_{0.47}Rh_{0.53}$/8 nm Pt Hall crosses at 298 K. (a) Schematic of the measurement. We make electrical contact to the crosses in an L-shape, therefore we measure m_x in the vertical branch and m_y in the horizontal branch. (b) The vertical branch at $H_{app} = \pm 2.4$ kOe along $+x$. The average between images at positive and negative field shows magnetization from pinned uncompensated moments that are unaffected by field, while the half-difference originates from unpinned uncompensated moments that reverse with field. (c) Imaging the horizontal branch. Only pinned magnetization appears in the ANE image, since the unpinned moments rotate to be parallel to $H_{app} \parallel x$ and we measure m_y in the horizontal branch.

it does not originate from simple ferromagnetism. We can rule out possible spurious contributions from spatial inhomogeneity in sample resistivity or thermal conductivity, for two reasons. First, spatially inhomogeneities produce characteristic dipole-like patterns in the V_{ANE} images from the charge Seebeck effect, which we do not observe[33]. Second, the inhomogeneous contrast disappears above the transition temperature T_C (see Appendix B). The images are reproducible in detail upon repeated heating and cooling cycles (see Appendix

E).

We distinguish the portion of the signal that has switched at $H_{app} = \pm$ 2.4 kOe from the portion that is unaffected by taking the half-difference and average, respectively. Meanwhile, the average V_{ANE} between positive and negative field is unaffected up to $H_{app} = \pm 5.2$ kOe, the largest field we can apply in our setup. Fig. 1(c) shows that the signal in the horizontal branch does not switch, as expected, because the moments that switch align with $H \parallel \hat{x}$, whereas we measure m_y here.

We attribute the micron-size regions of positive and negative V_{ANE} in Fig. 1(b) and (c) that do not switch with field to pinned uncompensated moments that are strongly coupled to the bulk Néel order. By definition pinned UMs carry a magnetic moment, therefore they should contribute an anomalous Nernst signal. Another potential source of V_{ANE} is supercooled FM domains from a magnetic glass state, which has been reported in Fe-rich FeRh[34]. However, $M(T)$ measurements of the phase transition in Fig. 3 do not show kinetic arrest in the cooling branch and $M(T)$ in the AF phase below room temperature (shown in Appendix C) does not exhibit field-cooling-dependent thermodynamic irreversibility, both of which are characteristic signs of a magnetic glass. We therefore rule out this possibility.

Pinned UMs can occur both in the bulk and at the interfaces of the AF. They can arise either within AF domain walls, or within AF domains from an Imry-Ma-type statistical imbalance in the number of defects in each of the two spin sublattices[5]. We can rule out AF domain walls as the dominant source of V_{ANE}, because AF domain walls are typically tens of nanometers wide[35] and would not be resolvable with our 650-nm resolution. In the Imry-Ma mechanism each AF domain carries a small net magnetization collinear with the Néel order. AF domains in FeRh thin films range between 300 nm and 2 μm in size depending on the defect density and growth methods[35], which is consistent with the 1-2 μm domains in the V_{ANE} images in Fig. 1(b) and 1(c). Nevertheless, we cannot directly confirm that V_{ANE} originates from magnetized AF domains without corresponding XMLD-PEEM images of the AF domains of the same sample, which suggests a direction for further experiments.

The contrast in the half-difference image in Fig. 1(b), representing moments that switch with magnetic field, could originate from unpinned UMs in the AF bulk and interfaces[36], or from an interfacial residual FM phase distinct from the AF bulk, which is common in FeRh thin films. Residual FM can occur at both the top and bottom interface[37] and has been variously attributed to strain[38], surface symmetry breaking[39], and chemical diffusion[40]. All these

sources of residual FM signal listed could contribute to V_{ANE}. However, previous studies of the effects of capping layers found no residual FM phase at the compensated FeRh(001)/Pt interface[40], which suggests that if there is a residual FM phase it most likely occurs at the bottom rather than the top interface. Regardless, its presence does not significantly affect our conclusions.

C. Local vertical exchange bias below T_C

To investigate the temperature dependence of pinned and unpinned UMs below T_C, we plot V_{ANE} images of the same sample as in Fig. 1 at $H_{app} = 1.3$ kOe at 298 K in Fig. 2(a) and 363 K in Fig. 2(b). We identify two adjacent magnetized AF domains, outlined in red and cyan line, using the zero crossing at zero magnetic field as the perimeter. We compute the average V_{ANE} of all pixels within these two domains as a function of H_{app} from -5.2 kOe to 5.2 kOe in increments of 1.3 kOe, and plot these averages at 298 K in Fig. 2(c) and at 363 K in Fig. 2(d). At 298 K, we obtain ferromagnetic hysteresis loops that are vertically shifted, enough to move the entire loop above or below zero, while at 363 K the contrast is more uniform and the magnitude of the vertical shifts decreases from 10 μV to ~ 4 μV.

Temperature-dependent vertical shifts and coercivity enhancement are the experimental signatures of *vertical* exchange bias[41,42], which is less common than the usual horizontal exchange bias in AF/FM bilayers. In horizontal EB, the moment originates from the FM and the horizontal shift yields the effective field from exchange coupling to the AF. In vertical EB, however, the vertical shift directly reflects the moment from the pinned UMs. Because the net moment from pinned UMs in the AF layer is typically much smaller than the moment from the FM layer, vertical EB is rarely observed in bulk magnetization measurements and usually requires either imaging[17] or depth-sensitive techniques such as XMCD[14,43] or x-ray reflectivity[44] to detect. In our images there is no large FM background, therefore we are able to resolve relatively weak moments from pinned UMs (V_{ANE} at 298 K is about 15 times smaller than in the full FM phase at 405 K).

Our V_{ANE} images are consistent with bulk magnetization measurements in the AF phase, presented in Appendix C. Bulk $M(H)$ measurements show a weak moment in the AF phase with coercive field $H_C = 470$ Oe at both 300 K and 360 K. This is consistent with Fig. 2(c) and (d) showing the UMs have switched at ± 1.3 kOe, since 1.3 kOe was the lowest nonzero

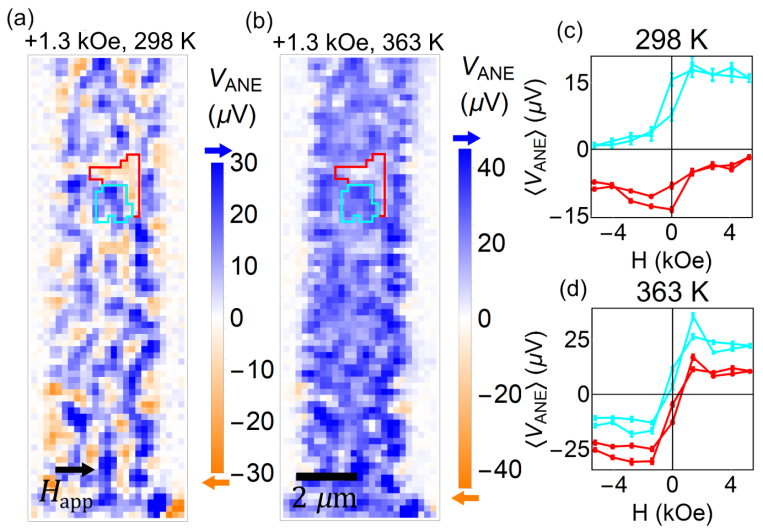

FIG. 2: Temperature dependence of the contrast from uncompensated moments in the AF phase. (a, b): ANE images of the 3-μm-wide Hall cross in Fig. 1, at (a) 298 K and (b) 363 K, at $H_{app} = 1.3$ kOe applied along $+x$. Cyan and red line outline adjacent AF domains, each containing a net *pinned* moment. (c,d) Average V_{ANE} of all pixels within the cyan and red outlined domains as a function of H_{app}, at 298 K (c) and 363 K (d). Ferromagnetic hysteresis loops with vertical shifts show *vertical* exchange bias from exchange coupling between the UMs and the bulk Néel order. At 363 K the magnitude of the vertical shifts decreases as some of the pinned UMs become unpinned.

field at which we performed ANE imaging. In the FM phase we find $H_C = 170$ Oe with bulk VSM and $H_C = 50$ Oe locally by measuring $V_{ANE}(H)$. Greater H_C in the AF than in the FM phase suggests that the unpinned UMs are exchange-coupled to the AF bulk and is consistent with a modified Stoner-Wolfarth model of uncompensated moments[45,46] in which varying degrees of exchange-coupling result in fully rotatable (unpinned) UMs, partially pinned UMs which enhance the coercivity, and fully pinned UMs which do not rotate at all with magnetic field. At 363 K the vertical shifts in Fig. 2(d) decrease, but H_C does not change. This suggests that at 363 K some pinned moments have become unpinned, but the magnitude of exchange-coupling between the bulk AF and the pinned UMs has not decreased.

III. CHARACTERIZING THE MAGNETIC PHASE TRANSITION

Before imaging the magnetic phase transition with ANE microscopy, we characterize the transition globally with $M(T)$ and electrical resistance $R(T)$ as well as locally with $V_{ANE}(T)$.

Since the resistivity decreases in the FM phase[47], both $R(T)$ and $M(T)$ are measures of the phase transition. We measure $M(T)$ of an unpatterned $Fe_{0.47}Rh_{0.53}$ film in Fig. 3(a) and $R(T)$ in a 20 μm $\times$ 100 μm four-terminal Hall bar in Fig. 3(b). We perform both measurements using a Quantum Design Physical Property Measurement System (PPMS), which has a maximum accessible temperature of 400 K. This temperature is not sufficient to induce the phase transition in our samples; however, by applying a magnetic field we can lower T_C[48]. We thus reach the FM phase by using a combination of magnetic field – 5.5 T in Fig. 3(a) and (b) – and 395 K temperature. We determine T_C from $M(T)$ as the temperature above which $M(T)$ is constant (i.e. $dM/dT = 0$), and separately from $R(T)$ as the temperature above which $R(T)$ is linear (dR/dT is constant); these two measurements of T_C agree within experimental error. In Fig. 3(c) we plot T_C measured with both $M(T)$ and $R(T)$ as a function of H_{app}. A linear fit yields a slope of 7.4 K/T, from which we extrapolate $T_C \approx 430$ K at $H_{app} = 0$.

We characterize the transition locally by measuring $V_{ANE}(T)$ at one point on a device in Fig. 3(d) with $H_{app} = 2$ kOe magnetic field, obtaining $T_C \approx 405$ K. We show in Appendix G that 3 mJ/cm^2 laser fluence heats the FeRh layer by a maximum transient $\Delta T = 15$ K, which is one contribution to the 25 K difference between T_C measured with V_{ANE} and $T_C \approx 430$ K extrapolated from $M(T)$ and $R(T)$. The remaining 10 K difference may be due to sample inhomogeneities and defects, which increase bulk T_C, as well as temperature fluctuations during V_{ANE} measurement from both the laser and the ambient heater. Inhomogeneities also contribute to the narrower transition hysteresis between heating and cooling branches measured with V_{ANE} (8 K) than with $M(T)$ and $R(T)$ ($\sim$30 K).

IV. INTERACTION OF COEXISTING ANTIFERROMAGNETIC AND FERROMAGNETIC PHASES NEAR T_C

A. ANE imaging through the phase transition

We next perform ANE imaging as a function of temperature and magnetic field through the phase transition, in which AF and FM order coexist. We image both heating and cooling portions of the transition, first at $H_{app} = +2$ kOe and then $H_{app} =$ -2 kOe applied along the x-axis, which are shown in Fig. 4(a) and Fig. 4(b), respectively.

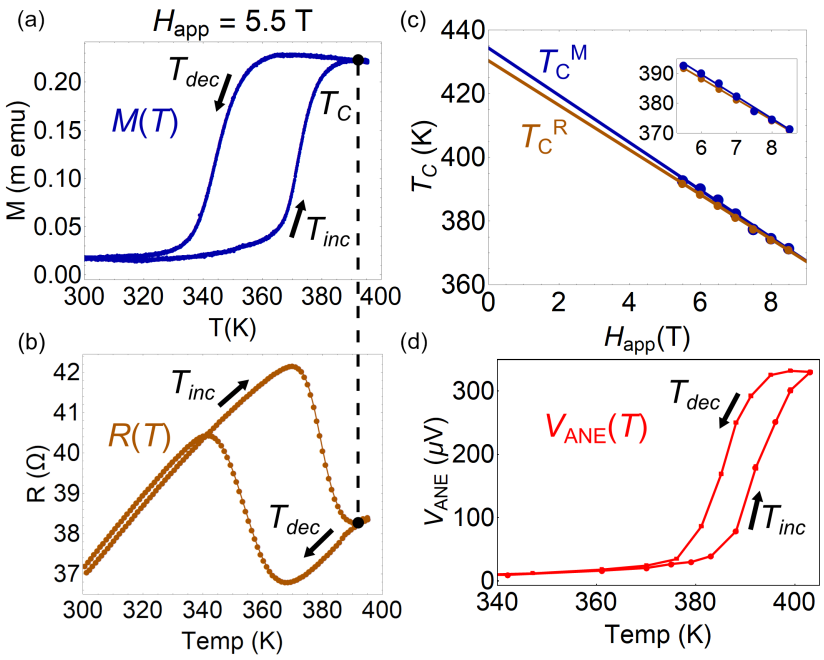

FIG. 3: Characterizing the magnetic phase transition. The heating and cooling branches of the transition are labeled with T_{inc} and T_{dec}, respectively. (a,b) Bulk moment $M(T)$ and electrical resistance $R(T)$ of a 4-terminal Hall bar, measured at applied field $H_{app} = 5.5$ T. $M(T)$ and $R(T)$ yield the same bulk transition temperature T_C within experimental error. (c) T_C determined by $M(T)$ and $R(T)$ as a function of H_{app}. We determine that T_C is linear in H_{app} with a slope of 7.4 K/T, from which we extrapolate $T_C(H_{app} = 0) = 430$ K. (d) $V_{ANE}(T)$ at one point on a FeRh/Pt device. Due to laser heating T_C measured with V_{ANE} is $\sim$ 405 K, about 25 K lower than than T_C measured with $M(T)$ and $R(T)$.

The ANE images through the transition show that the FM phase nucleates, percolates, and coalesces, in agreement with previous imaging studies in FeRh[35,37,49,50]. At 365 K the contrast shows UMs and residual FMs in the AF phase. We observe FM domains nucleating first at sample edges and defects at 376 K and 381 K, percolating through the device at 385 K until V_{ANE} is nearly uniform in the FM phase at 399 K. Unexpectedly, we find that some of the FM domains nucleate with an orientation that is not parallel to the applied field, even though $H_{app} = 2$ kOe is much greater than the local $H_C = 50$ Oe in the FM phase (see Appendix C). At 381 K in Fig. 4(a), the moments on the edges tend to have positive m_x (blue), parallel to H_{app}, while the moments near the center of the device tend to have *negative* m_x (orange), *opposite* to H_{app}. At H_{app} = -2 kOe in Fig. 4(b) we observe the same phenomenon: the orange moments at the edges tend to be parallel to H_{app} and the blue moments in the middle tend to be opposite to H_{app}. As the FM moments coalesce above

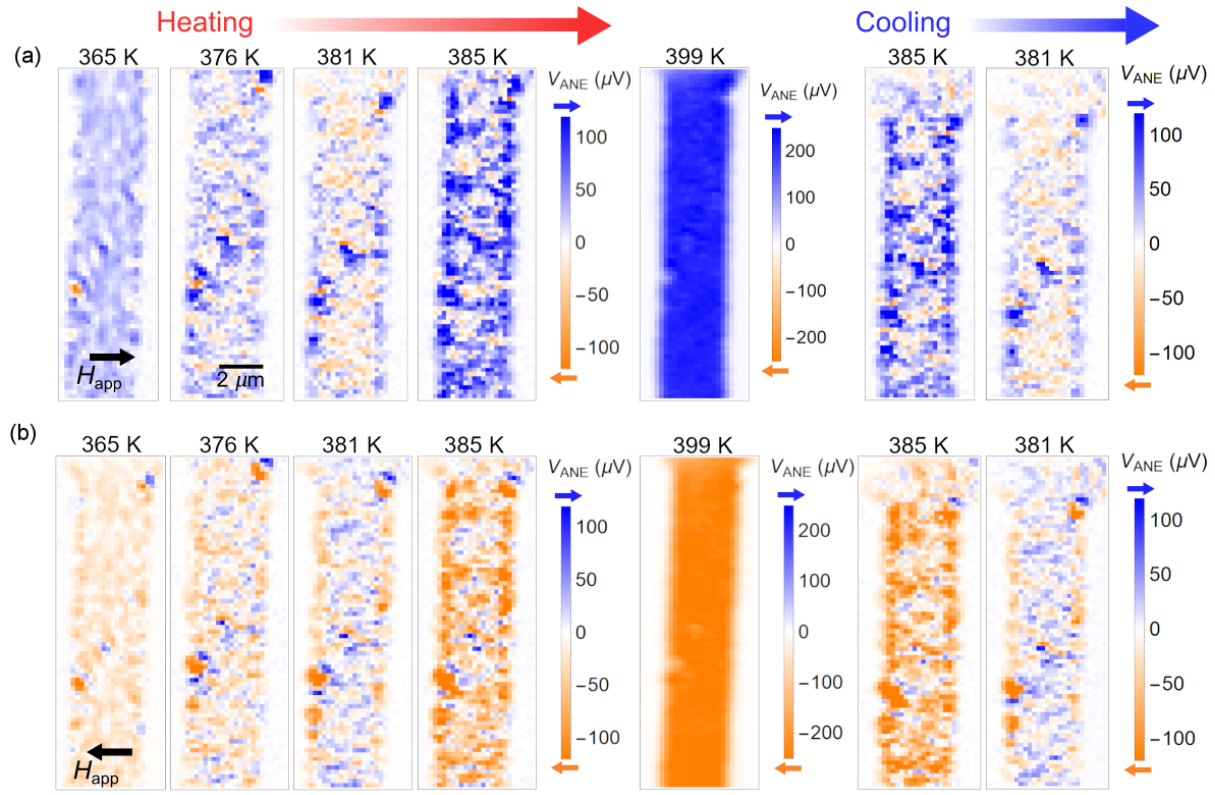

FIG. 4: Imaging the metamagnetic phase transition from AF to FM. (a) ANE imaging of the transition at H_{app} = 2 kOe applied along $+x$. We observe nucleation, percolation, and growth of FM domains, characteristic of the 1st-order transition. Surprisingly, the emergent FM domains at 381 K are oriented opposite to H_{app}, indicating that they are exchange-coupled to the bulk Néel order. (b) Imaging the transition again at H_{app} = -2 kOe. Again the FM domains nucleate oriented opposite to H_{app}, which suggests that the exchange-coupling J_{F-AF} between emergent FM and bulk AF is antiferromagnetic.

385 K, they reorient to be parallel to the applied field for both orientations of H_{app}. The spatial structure in the heating branch reproduces in the cooling branch, seen by comparing the corresponding heating and cooling images at 385 K and 381 K.

We explain these puzzling results in terms of exchange bias between FM interfaces and the AF bulk within the FeRh film near T_C. Previous cross-sectional imaging of the phase transition in FeRh with electron holography showed that the transition occurs first at the top and bottom interfaces before spreading into the bulk[37]. Therefore, for some temperature range near T_C the interfaces of the FeRh film are FM while the bulk is still AF, forming a kind of AF/FM heterostructure with rough interfaces. Our observation of newly nucleated FM domains that are not parallel to H_{app}, even when H_{app} = 2 kOe is greater than both H_C = 50 Oe in the FM phase and H_C = 470 Oe in the AF phase, indicates that the

FM interfaces are pinned by exchange-coupling to the pinned UMs; in other words, the FM interfaces are exchange-biased by the AF bulk as previously suggested by spin wave resonance measurements in Pd-doped FeRh[51].

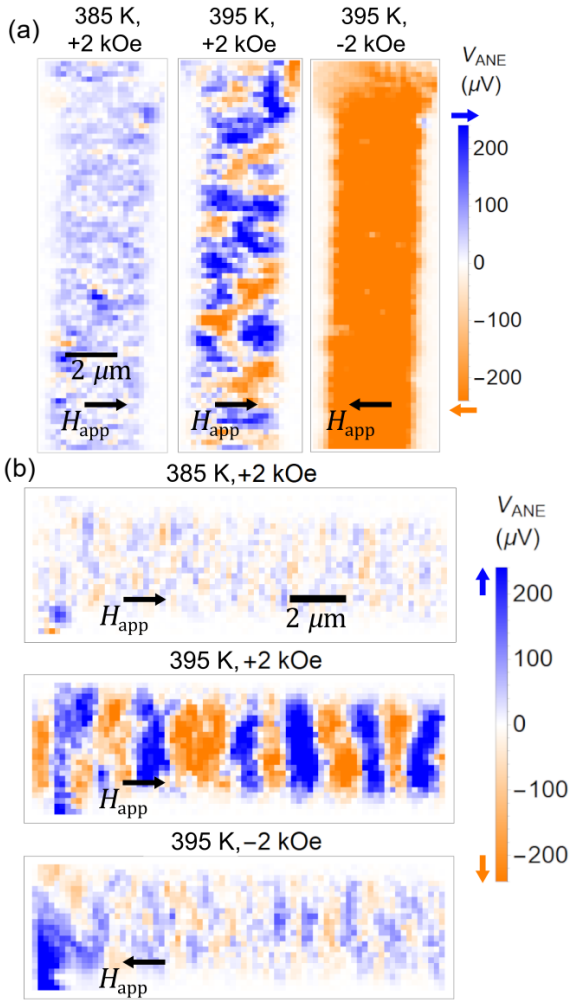

FIG. 5: Metastable states of of FM domains pinned in different in-plane orientations, even in the presence of nominally saturating H_{app} = 2 kOe applied field. (a) In the same Hall cross as in Fig. 4, we observe emergent FM domains pinned towards and opposite H_{app} at 395 K, which collapse into the uniform FM state after reversing the direction of H_{app}. (b) Corresponding images of the horizontal branch of the same cross, acquired simultaneously as (a). At 395 K and H_{app} = +2 kOe we observe large-scale emergent FM domains oriented perpendicular to H_{app}. Weak contrast at H_{app} = -2 kOe shows that the magnetic structure collapses into the uniform FM state, oriented along $-x$.

B. Exchange-biased FM domains near T_C

To observe both m_x and m_y near T_C, in Fig. 5(a) and 5(b) we image the vertical and horizontal branch of the same device as in Fig. 4. At 385 K and $H_{app} = +2$ kOe magnetic field applied along the x-direction, we observe mostly positive V_{ANE} in the vertical branch and weak contrast in the horizontal branch. V_{ANE} at this temperature represents unpinned UMs parallel to H_{app}. At 395 K and $H_{app} = 2$ kOe, however, we observe the sudden emergence of large-scale (> 2 μm) FM domains of positive and negative V_{ANE} in both the vertical and horizontal branch. Because we measure m_x in the vertical branch and m_y in the horizontal branch, this data shows simultaneously existing FM domains with positive and negative projections in both x and y. These FM domains could result from multiple simultaneously acting exchange biases: depending on the mechanism, the exchange coupling between the FM moments and the pinned UMs can be parallel[52], antiparallel[53], or perpendicular[54]. According to this explanation, V_{ANE} in the vertical and horizontal branches in Fig. 5 is due to collinear and perpendicular EB, respectively, since different directions of EB can coexist simultaneously[43,55]. Another possibility, since the antiferromagnetic easy axes are at 45° with respect to the device edges, is that the FM domains at the interfaces are forced by exchange-coupling to the AF bulk to lie along the four 45° directions within the xy-plane. In this case only a single mechanism of EB – that is, a single orientation of the FM domains with respect to the AF domains – is necessary to account for positive and negative V_{ANE} in both branches. Since V_{ANE} depends on both the magnitude and direction of $\boldsymbol{m}$ and these two quantities both vary near T_C, we cannot determine the absolute direction of $\boldsymbol{m}$ within the present experimental framework.

Imaging another 3 μm-wide device from the same film at $H_{app} = 2.0$ kOe applied field in Fig. 6(a) while measuring the resistance in 6(b) shows even more puzzling behavior. At 388 K we observe unpinned UMs in the AF phase, oriented parallel to H_{app}. At 394 K, maintaining H_{app} at +2.0 kOe, we see that the moments in the upper portion of the channel are mostly pinned opposite H_{app}, while the moments in the lower third are parallel to H_{app}. Upon immediately retaking the image, the entire sample has collapsed into the FM phase parallel to H_{app}, accompanied by a sharp decrease of the resistance in Fig. 6(b) which indicates the transition into the FM phase. This data is reproducible as shown in Appendix F, and additionally because the raster scanning proceeds from bottom to top, the spatial

phase inhomogeneity is not due to the sample collapsing into the FM phase during the 20-30 min process of imaging. The spatial inhomogeneity and sudden collapse of the exchange-biased AF/FM heterostructure shows that the states of exchange-biased interfacial FM and bulk AF are metastable and suggests (but does not prove) that in this case the transition is avalanche-like[56] and proceeds by front propagation[57].

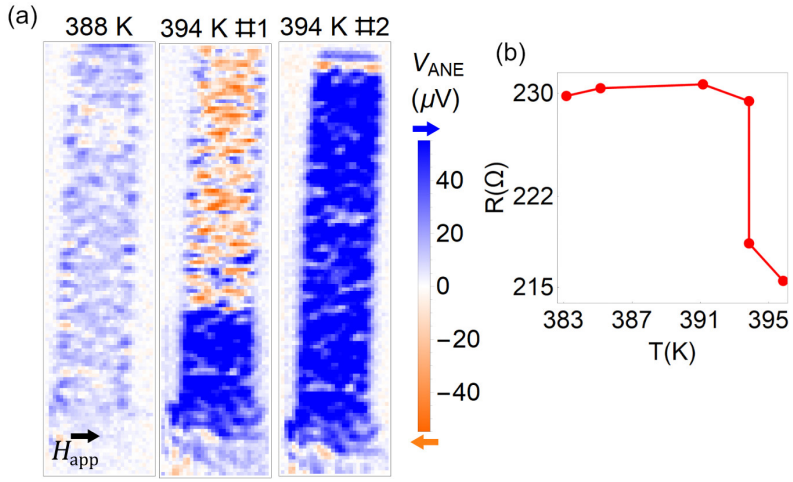

FIG. 6: Spatially inhomogeneous collapse of metastable exchange-coupled states on a similar device as in Fig. 5. At 394 K and $H_{app} = 2.0$ kOe along $+x$ we image unpinned UMs and residual FM. At 394 K the lower portion of the cross is uniformly FM parallel to H_{app}, while the upper portion is an exchange-biased mixture of AF and FM. Immediately imaging again causes the FM to collapse uniformly parallel to H_{app}, suggesting an avalanche-like transition proceeding by front propagation. (b) Sample resistance during the imaging in (a). The resistance decreases suddenly at the point of the collapse of exchange bias.

Although we do not have a comprehensive understanding of the complicated patterns of exchange bias near T_C, we can gain insight by imaging while varying the applied field H_{app}, the cooling field H_{FC} after heating 10 K above T_C, and the laser fluence f. A full set of data is presented in Appendix F, however, we summarize the most important conclusions here. We observe similar spatial patterns of FM domains for both $H_{FC} = +2$ kOe and -2 kOe, which indicates that the EB is unaffected by H_{FC}. We also observe similar patterns for both $H_{app} = 100$ Oe and $H_{app} = 2$ kOe, which indicates that the EB does not depend on the magnitude of H_{app} as long as $H_{app} > H_C$ in the FM phase. We only observe large-scale FM domains opposite and perpendicular to H_{app} for fluence $f = 1.9$ mJ/cm^2, which causes a maximum transient temperature increase $\Delta T = 10$ K, and above. One possible explanation is that the pulsed laser anneals the magnetic structure. The laser initially unpins the pinned UMs, and after repeated heating and cooling from many pulses they

become pinned parallel to H_{app}[58], rotating the emergent FM spins opposite to H_{app}[59] in a similar manner to training-induced positive exchange bias[52]. Similar behavior could be induced if the temperature fluctuates above and below T_C: a short-lived FM state orients parallel to H_{app}, which affects the Néel orientation in the AF phase, which further affects the FM domain orientation. Further studies varying the number of pulses delivered to each pixel may be necessary to distinguish these mechanisms.

V. CONCLUSION

In summary, we use anomalous Nernst microscopy to image uncompensated moments in the AF phase of FeRh below T_C as well as emergent FM near T_C. We resolve enhanced coercivity and spatially inhomogeneous vertical exchange bias below T_C, demonstrating varying degrees of exchange-coupling between UMs and the bulk Néel order. In addition, we demonstrate that newly nucleated FM domains near T_C are exchange-coupled to the pinned UMs even in the presence of a nominally saturating magnetic field, providing a direct experimental demonstration of exchange bias within a single FeRh thin film. We expect the imaging of uncompensated moments with anomalous Nernst microscopy to extend to a variety of AF metals, which could lead to a better understanding of the role of bulk UMs on exchange bias in both pure AFs and AF/FM bilayers.

VI. ACKNOWLEDGMENTS

This research was primarily supported by the Cornell Center for Materials Research with funding from the NSF MRSEC program (DMR-1719875). This work made use of the CCMR Shared Facilities and the Cornell NanoScale Facility, an NNCI member supported by NSF Grant ECCS-1542081. A.B.M. and D.G.S. acknowledge support in part by the Semiconductor Research Corporation (SRC) under nCORE task 2758.003 and by the NSF under the E2CDA program (ECCS-1740136). G.M.S. acknowledges support by the National Science Foundation (DMR-1708499). Materials synthesis was performed in part in a facility supported by the National Science Foundation [Platform for the Accelerated Realization, Analysis, and Discovery of Interface Materials (PARADIM) under Cooperative Agreement

No. DMR-1539918.

[1] L. Néel, Science **174**, 985 (1971).

[2] P. Miltényi, M. Gierlings, J. Keller, B. Beschoten, G. Güntherodt, U. Nowak, and K. Usadel, Phys. Rev. Lett. **84**, 4224 (2000).

[3] J. S. White, M. Bator, Y. Hu, H. Luetkens, J. Stahn, S. Capelli, S. Das, M. Döbeli, T. Lippert, V. K. Malik, J. Martynczuk, A. Wokaun, M. Kenzelmann, C. Niedermayer, and C. W. Schneider, Phys. Rev. Lett. **111**, 037201 (2013).

[4] M. Charilaou and F. Hellman, J. Appl. Phys. **117** (2015).

[5] Y. Imry and S.-K. Ma, Phys. Rev. Lett. **35**, 1399 (1975).

[6] H. Rohrer and H. J. Scheel, Phys. Rev. Lett. **44**, 876 (1980).

[7] Note that we use the term *uncompensated moment* to mean a net magnetization from uncompensated spins, not the individual spins themselves.

[8] J. Nogués and I. K. Schuller, Journal of Magnetism and Magnetic Materials **192**, 203 (1999).

[9] I. K. Schuller, R. Morales, X. Batlle, U. Nowak, and G. Güntherodt, Journal of Magnetism and Magnetic Materials **416**, 2 (2016).

[10] C. Reig, M.-D. Cubells-Beltrán, and D. R. Muñoz, Sensors **9**, 7919 (2009).

[11] W. H. Meiklejohn and C. P. Bean, Physical Review **102** (1957).

[12] R. Jungblut, R. Coehoorn, M. T. Johnson, J. aan de Stegge, and A. Reinders, Journal of Applied Physics **75**, 6659 (1994).

[13] K. Takano, R. H. Kodama, A. E. Berkowitz, W. Cao, and G. Thomas, Phys. Rev. Lett. **79**, 1130 (1997).

[14] S. Brück, G. Schütz, E. Goering, X. Ji, and K. M. Krishnan, Phys. Rev. Lett. **101**, 126402 (2008).

[15] U. Nowak, K. D. Usadel, J. Keller, P. Miltényi, B. Beschoten, and G. Güntherodt, Phys. Rev. B **66**, 014430 (2002).

[16] J. Nogués, C. Leighton, and I. K. Schuller, Phys. Rev. B **61**, 1315 (2000).

[17] P. Kappenberger, S. Martin, Y. Pellmont, H. J. Hug, J. B. Kortright, O. Hellwig, and E. E. Fullerton, Phys. Rev. Lett. **91**, 267202 (2003).

[18] J. Miguel, R. Abrudan, M. Bernien, M. Piantek, C. Tieg, J. Kirschner, and W. Kuch, Journal of Physics: Condensed Matter **21**, 185004 (2009).

[19] J. B. McKinnon, D. Melville, and E. W. Lee, Journal of Physics C: Solid State Physics **3**, S46 (1970).

[20] M. Wolloch, M. E. Gruner, W. Keune, P. Mohn, J. Redinger, F. Hofer, D. Suess, R. Podloucky, J. Landers, S. Salamon, F. Scheibel, D. Spoddig, R. Witte, B. Roldan Cuenya, O. Gutfleisch, M. Y. Hu, J. Zhao, T. Toellner, E. E. Alp, M. Siewert, P. Entel, R. Pentcheva, and H. Wende, Phys. Rev. B **94**, 174435 (2016).

[21] Z. Q. Liu, L. Li, Z. Gai, J. D. Clarkson, S. L. Hsu, A. T. Wong, L. S. Fan, M.-W. Lin, C. M. Rouleau, T. Z. Ward, H. N. Lee, A. S. Sefat, H. M. Christen, and R. Ramesh, Phys. Rev. Lett. **116**, 097203 (2016).

[22] G. Zheng, S.-H. Ke, M. Miao, J. Kim, R. Ramesh, and N. Kioussis, Scientific Reports **7**, 5366 (2017).

[23] R. O. Cherifi, V. Ivanovskaya, L. C. Phillips, A. Zobelli, I. C. Infante, E. Jacquet, V. Garcia, S. Fusil, P. R. Briddon, N. Guiblin, A. Mougin, A. A. Ünal, F. Kronast, S. Valencia, B. Dkhil, A. Bartélémy, and M. Bibes, Nature Materials **13**, 345 (2014).

[24] J.-U. Thiele, S. Maat, J. L. Robertson, and E. E. Fullerton, IEEE Transactions on Magnetics **40**, 2537 (2004).

[25] M. Weiler, M. Althammer, F. D. Czeschka, H. Huebl, M. S. Wagner, M. Opel, I.-M. Imort, G. Reiss, A. Thomas, R. Gross, and S. T. B. Goennenwein, Phys. Rev. Lett. **108**, 106602 (2012).

[26] J. M. Bartell, D. H. Ngai, Z. Leng, and G. D. Fuchs, Nature Communications **6**, 8460 (2015).

[27] J. M. Bartell, C. L. Jermain, S. V. Aradhya, J. T. Brangham, F. Yang, D. C. Ralph, and G. D. Fuchs, Phys. Rev. Applied **7**, 044004 (2017).

[28] F. Guo, J. M. Bartell, and G. D. Fuchs, Phys. Rev. B **93**, 144415 (2016).

[29] F. Guo, J. M. Bartell, D. H. Ngai, and G. D. Fuchs, Phys. Rev. Applied **4**, 044004 (2015).

[30] I. Gray, T. Moriyama, N. Sivadas, G. M. Stiehl, J. T. Heron, R. Need, B. J. Kirby, D. H. Low, K. C. Nowack, D. G. Schlom, D. C. Ralph, T. Ono, and G. D. Fuchs, arXiv e-prints (2018), arXiv:1810.03997.

[31] R. Iguchi, S. Kasai, K. Koshikawa, N. Chinone, S. Suzuki, and K.-i. Uchida, arXiv e-prints , arXiv:1903.01037 (2019), arXiv:1903.01037 [cond-mat.mes-hall].

[32] In addition to FM LSSE from uncompensated moments, both bulk and interfacial AF LSSE are possible. However, we expect signal from AF LSSE to be linear in field (see *Wu et al, Phys. Rev. Lett.* ***116****, 097204 (2016)* and *Seki et al, Phys. Rev. Lett.* ***115****, 266601 (2015*), which is not present in the data. We can rule out interfacial AF LSSE because it relies on an uncompensated AF interface and the interface of FeRh(001) is compensated.

[33] A. B. Mei, I. Gray, Y. Tang, J. Schubert, D. Werder, J. Bartell, D. C. Ralph, G. D. Fuchs, and D. G. Schlom, arXiv e-prints , arXiv:1906.07239 (2019), arXiv:1906.07239 [cond-mat.mtrl-sci].

[34] J. Chen, Y. Gao, J. Ma, and C.-W. Nan, Materials Research Letters **5**, 329 (2017).

[35] C. Baldasseroni, C. Bordel, C. Antonakos, A. Scholl, K. H. Stone, J. B. Kortright, and F. Hellman, Journal of Physics: Condensed Matter **27**, 256001 (2015).

[36] D. Kande, D. Laughlin, and J.-G. Zhu, Journal of Applied Physics **107**, 09E318 (2010).

[37] C. Gatel, B. Warot-Fonrose, N. Biziere, L. A. Rodríguez, D. Reyes, R. Cours, M. Castiella, and M. J. Casanove, Nature Communications **8**, 15703 (2017).

[38] R. Fan, C. J. Kinane, T. R. Charlton, R. Dorner, M. Ali, M. A. de Vries, R. M. D. Brydson, C. H. Marrows, B. J. Hickey, D. A. Arena, B. K. Tanner, G. Nisbet, and S. Langridge, Phys. Rev. B **82**, 184418 (2010).

[39] F. Pressacco, V. Uhlir, M. Gatti, A. Bendounan, E. E. Fullerton, and F. Sirotti, Scientific Reports **6** (2016).

[40] C. Baldasseroni, G. K. Plsson, C. Bordel, S. Valencia, A. A. Unal, F. Kronast, S. Nemsak, C. S. Fadley, J. A. Borchers, B. B. Maranville, and F. Hellman, Journal of Applied Physics **115**, 043919 (2014), https://doi.org/10.1063/1.4862961.

[41] R. K. Zheng, G. H. Wen, K. K. Fung, and X. X. Zhang, Journal of Applied Physics **95** (2004).

[42] E. C. Passamani, C. Larica, C. Marques, J. R. Preveti, A. Y. Takeuchi, and F. H. Sanchez, Journal of Magnetism and Magnetic Materials **299**, 11 (2006).

[43] H. Ohldag, H. Shi, E. Arenholz, J. Stöhr, and D. Lederman, Phys. Rev. Lett. **96**, 027203 (2006).

[44] M. Gruyters and D. Schmitz, Phys. Rev. Lett. **100**, 077205 (2008).

[45] B. Henne, V. Ney, M. de Souza, and A. Ney, Phys. Rev. B **93**, 144406 (2016).

[46] M. Buchner, B. Henne, V. Ney, and A. Ney, Phys. Rev. B **99**, 064409 (2019).

[47] M. Sharma, H. M. Aarbogh, J. U. Thiele, S. Maat, E. E. Fullerton, and C. Leighton, Journal of Applied Physics **109**, 083913 (2011).

[48] S. Maat, J.-U. Thiele, and E. E. Fullerton, Phys. Rev. B **72**, 214432 (2005).

[49] C. Baldasseroni, C. Bordel, A. X. Gray, A. M. Kaiser, F. Kronast, J. Herrero-Albillos, C. M. Schneider, C. S. Fadley, and F. Hellman, Applied Physics Letters **100**, 262401 (2012).

[50] T. P. Almeida, R. Temple, J. Massey, K. Fallon, D. McGrouther, T. Moore, C. H. Marrows, and S. McVitie, Scientific Reports **7**, 17835 (2017).

[51] J. R. Massey, K. Matsumoto, M. Strungaru, R. C. Temple, T. Higo, K. Kondou, R. F. L. Evans, G. Burnell, R. W. Chantrell, and Y. Otani, arXiv e-prints , arXiv:1807.01615 (2018), arXiv:1807.01615 [cond-mat.mtrl-sci].

[52] J. Nogués, D. Lederman, T. J. Moran, and I. K. Schuller, Phys. Rev. Lett. **76**, 4624 (1996).

[53] M. Grimsditch, A. Hoffmann, P. Vavassori, H. Shi, and D. Lederman, Phys. Rev. Lett. **90**, 257201 (2003).

[54] S. Maat, K. Takano, S. S. P. Parkin, and E. E. Fullerton, Phys. Rev. Lett. **87**, 087202 (2001).

[55] F. Radu, M. Etzkorn, R. Siebrecht, T. Schmitte, K. Westerholt, and H. Zabel, Phys. Rev. B **67**, 134409 (2003).

[56] L. Carrillo and J. Ortín, Phys. Rev. B **56**, 11508 (1997).

[57] J. A. Shaw and S. Kyriakides, Acta Materialia **45**, 683 (1997).

[58] G. Salazar-Alvarez, J. J. Kavich, J. Sort, A. Mugarza, S. Stepanow, A. Potenza, H. Marchetto, S. S. Dhesi, V. Baltz, B. Dieny, A. Weber, L. J. Heyderman, J. Nogués, and P. Gambardella, Applied Physics Letters **95**, 012510 (2009), https://doi.org/10.1063/1.3168515.

[59] J. Sort, K. S. Buchanan, V. Novosad, A. Hoffmann, G. Salazar-Alvarez, A. Bollero, M. D. Baró, B. Dieny, and J. Nogués, Phys. Rev. Lett. **97**, 067201 (2006).

[60] A. B. Mei, Y. Tang, J. L. Grab, J. Schubert, D. C. Ralph, and D. G. Schlom, Applied Physics Letters **113**, 082403 (2018).

[61] G. Shirane, C. W. Chen, P. A. Flinn, and R. Nathans, Phys. Rev. **131**, 183 (1963).

[62] N. Nagaosa, J. Sinova, S. Onoda, A. H. MacDonald, and N. P. Ong, Rev. Mod. Phys. **82**, 1539 (2010).

[63] X. Marti, I. Fina, J. Liu, P. Wadley, Q. He, R. Paull, J. Clarkson, J. Kudrnovský, I. Turek, Kuneš, D. Yi, J.-H. Chu, C. Nelson, L. You, E. Arenholz, S. Salahuddin, J. Fontcuberta, T. Jungwirth, and R. Ramesh, Nature Materials **13**, 367 (2014).

[64] T. Moriyama, N. Matsuzaki, K.-J. Kim, I. Suzuki, T. Taniyama, and T. Ono, Applied Physics Letters **107**, 122403 (2015).

[65] A. Y.-C. Yu, W. E. Spicer, and G. Hass, Physical Review **171**, 834 (1968).

[66] L.-Y. Chen, *Optical properties of metals and alloys: Au, Ag, FeRh, AuAl2, and PtAl2*, Ph.D. thesis, Iowa State University (1987).

Appendix A: FeRh-Pt growth and characterization

The FeRh/Pt thin films in the main text were grown by DC sputtering from a stoichiometric $Fe_{0.49}Rh_{0.51}$ target onto single-crystal MgO(001) substrates. The base pressure was 2×10^{-8} torr. The samples were grown at 648 K and annealed at 793 K for 1 hour.

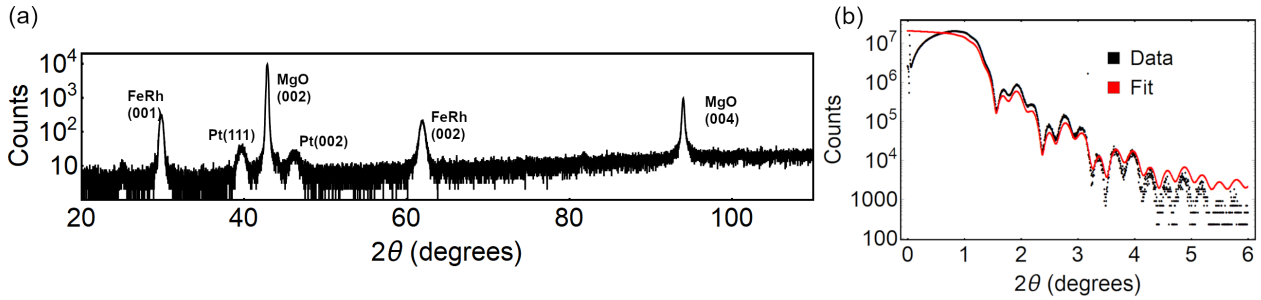

FIG. 7: Structural characterization of the MgO(001)/FeRh/Pt samples. (a) XRD scan demonstrating epitaxial growth of FeRh(001) on MgO(001). (b) XRR scan of the same film. From the fit we estimate the thicknesses of the FeRh and Pt layers to be 20.5 nm and 8.0 nm, respectively.

Fig. 7(a) shows the XRD scan of the MgO(001)/FeRh/Pt samples imaged in the main text. The FeRh(001) and (002) peaks demonstrate epitaxial growth of B2 CsCl FeRh(001). Previous structural characterization of ordered B2 CsCl FeRh as a function of growth composition[60] showed a linear relation between the Rh concentration and the strain in the AF phase, manifesting in the FeRh peak positions in the XRD. Using this linear relation we estimate the Fe and Rh concentrations to be 47% and 53%, respectively.

From the FeRh(002) peak at $2\theta = 61.9°$ we obtain an out-of-plane lattice constant of $a = 0.2996$ nm. This value is greater than the bulk value of 0.2986 nm for $Fe_{1-x}Rh_x$ with $52 < x < 60$[61], which indicates that the FeRh is compressively strained. Note that because the AF-FM phase transition is accompanied by a $\sim 1\%$ lattice expansion, the strain is greater in the FM phase than in the AF phase. This rules out the possibility that the contrast we attribute to pinned UMs in Fig. 1 and Fig. 2 of the main text is due to strain, and that the contrast disappears in the FM phase because the lattice expansion relaxes the strain.

Fig. 7(b) shows XRR data on the same FeRh/Pt film. From the fit we estimate the thicknesses of the FeRh and Pt layers as 20.5 nm and 8.0 nm, respectively, and the surface roughness to be 0.46 nm for both layers.

Appendix B: Disappearance of AF uncompensated moments in the FM phase

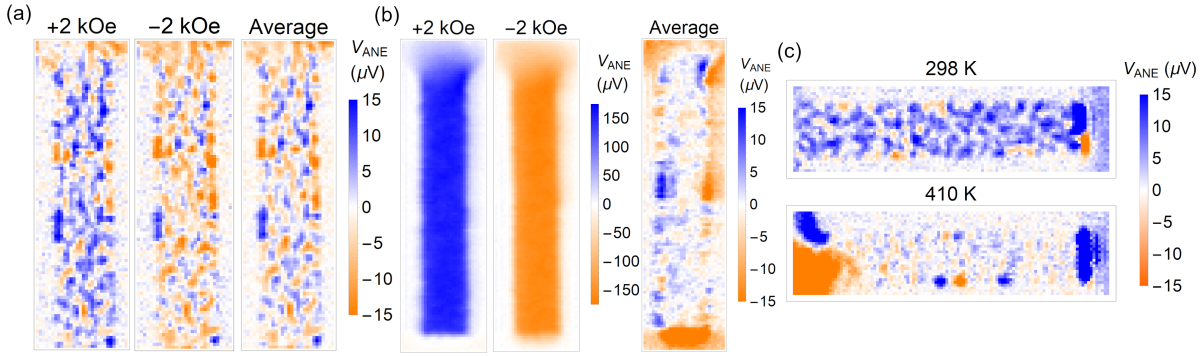

FIG. 8: Disappearance of the pinned UMs in the FM phase. (a) V_{ANE} imaging of the vertical branch of a 3 μm-wide Hall cross of $Fe_{0.47}Rh_{0.53}$/Pt in the AF phase at 298 K. The average between images at $H_{app} = \pm 2$ kOe shows pinned UMs as in Fig. 1 of the main text. (b) The same branch in the FM phase at 410 K. The average of $H_{app} = \pm 2$ kOe shows that the pinned UMs in the AF phase disappear in the FM phase; residual contrast near the edges may reflect imperfect image alignment. (b,c) The horizontal branch of the same cross, which we image at 295 K (b) and 410 K (c) to avoid artifacts from aligning two images. The pinned UMs that we observe at 298 K disappear in the FM phase at 410 K.

In this section we demonstrate that the micron-size regions of positive and negative V_{ANE} we image in the AF phase in FeRh vanish above T_C in the FM phase. In Fig. 8(a) we image the vertical branch of a 3 μm-wide Hall cross of $Fe_{0.47}Rh_{0.53}$/Pt, similar to the samples imaged in the main text. We first image at 298 K with $H_{app} = \pm 2.0$ kOe applied along x and take the average to show the pinned UMs. We then image at 410 K – in the FM phase – applying $H_{app} = \pm 2$ kOe, shown in Fig. 8(b). Plotting the average at 410 K on the same color scale as the average at 298 K shows that the structure of the pinned UMs at 298 K disappears in the FM phase. Contrast near the edges may arise from imperfect alignment between the two images. To avoid this issue, we image the horizontal branch of the same cross with $H_{app} = 2$ kOe applied along x in Fig. 8(c). Imaging at 298 K shows pinned UMs similar in structure to those shown in Fig. 1 of the main text. In the FM phase at 410 K, the contrast from UMs disappears because the FM moments are saturated along x and we

measure m_y in the horizontal branch.

Appendix C: Magnetometry of FeRh/Pt

In this section we characterize $M(H)$ and $M(T)$ of our FeRh/Pt samples. Fig. 9(a) shows $M(H)$ in the AF phase at 300 K and 360 K and in the FM phase at 395 K, taken with a VSM and a PPMS as in Fig. 3. We obtain coercive fields $H_C = 470$ Oe at both 300 K and 360 K. Although the saturation moments at 300 and 360 K are nearly identical, V_{ANE} increases by a factor of two in Fig. 2(c) and 2(d), which likely is due to an increase in the ANE coefficient with increasing temperature[62]. Since the maximum attainable temperature in the PPMS is 400 K, we drive the FeRh into the FM phase by applying 8.5 T at 395 K before reducing the field to measure $M(H)$, from which we obtain $H_C = 170$ Oe. We compare this bulk $M(H)$ to a local measurement of $V_{ANE}(H)$ in a FeRh/Pt device at 406 K in Fig. 9(b), in which $H_C \approx 50$ Oe. We expect that defects and pinning sites will cause bulk H_C to be higher than local H_C. In addition, although Fig. 3 shows that once reached the FM phase persists about 40 K below the bulk T_C, some AF domains may have reappeared at 395 K, which would increase H_C.

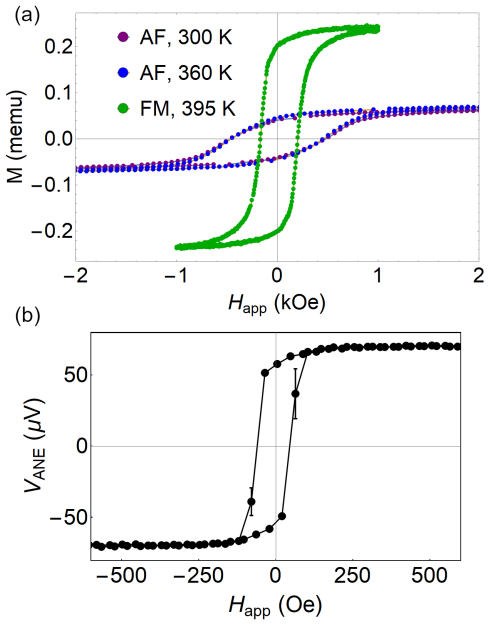

FIG. 9: (a) $M(H)$ on FeRh/Pt in the AF phase at 300 K and 370 K and in the FM phase at 395 K. We obtain $H_C = 470$ Oe in the AF phase and $H_C = 170$ Oe in the FM phase. (b) $V_{ANE}(H)$ – a local measure of $M(H)$ – in a FeRh/Pt device at 406 K. We obtain $H_C \approx 50$ Oe in the FM phase.

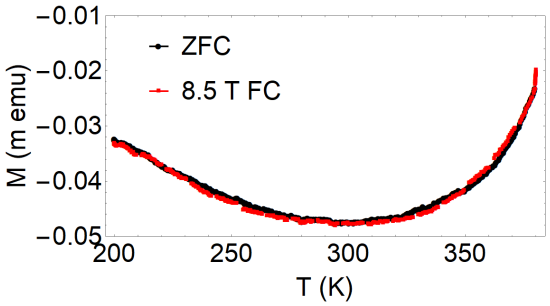

FIG. 10: $M(T)$ in the AF phase after cooling from above T_C at $H_{FC} = 0$ and $H_{FC} = 8.5$ T to test for thermodynamic irreversibility from a potential magnetic glass state in FeRh. The two curves overlap two within 0.2%, ruling out this state.

We additionally test the possibility of a magnetic glass state in our FeRh[34], in which supercooled FM domains persist in the AF phase due to kinetic arrest of the phase transition. These supercooled FM domains are an alternative possible source of V_{ANE} in addition to UMs in the AF phase. However, kinetic arrest produces asymmetry between the heating and cooling branches of $M(T)$, whereas we find $M(T)$ to be symmetric as seen in Fig. 3. We perform an additional test, shown in Fig. 10, by measuring $M(T)$ in the AF phase at $H_{app} = 2$ T. If the sample is accessing a magnetic glass state, field-cooling induces a vertical bifurcation between $M(T)$ after zero field-cooling and $M(T)$ after field-cooling (about 1% in Ref.[34]). We measure $M(T)$ after $H_{FC} = 0$ and $M(T)$ after $H_{FC} = 8.5$ T, and find no vertical offset between the two curves to within 0.2%. This null result is consistent with the fact that our samples are Rh-rich, whereas magnetic glasses were observed in Fe-rich FeRh[34]. We therefore rule out the possibility of a magnetic glass state as the dominant source of V_{ANE}.

Appendix D: ANE imaging of varying FeRh stoichiometry

In the main text we image FeRh capped with Pt. In addition to ANE within the FeRh bulk, a longitudinal spin Seebeck effect (LSSE) at the Pt/FeRh interface could contribute to the V_{ANE} voltage we measure, which would have the same symmetry as the ANE. To separate out any potential interfacial LSSE and explore the AF domain structure at different FeRh compositions, we image uncapped $Fe_{0.43}Rh_{0.57}$ and $Fe_{0.52}Rh_{0.48}$ in Fig. 11(a) and 11(b), respectively. Both samples are approximately 35 nm thick, grown on MgO(001) substrates. Note that while the FeRh/Pt films in the main text are sputtered, the $Fe_{0.43}Rh_{0.57}$

and $Fe_{0.52}Rh_{0.48}$ samples are grown by molecular-beam epitaxy. We image at positive and negative H_{app} applied along x and take the half-difference, following the same procedure as we do in the main text. We show both the horizontal and vertical branch of the $Fe_{0.43}Rh_{0.57}$ sample in the same image.

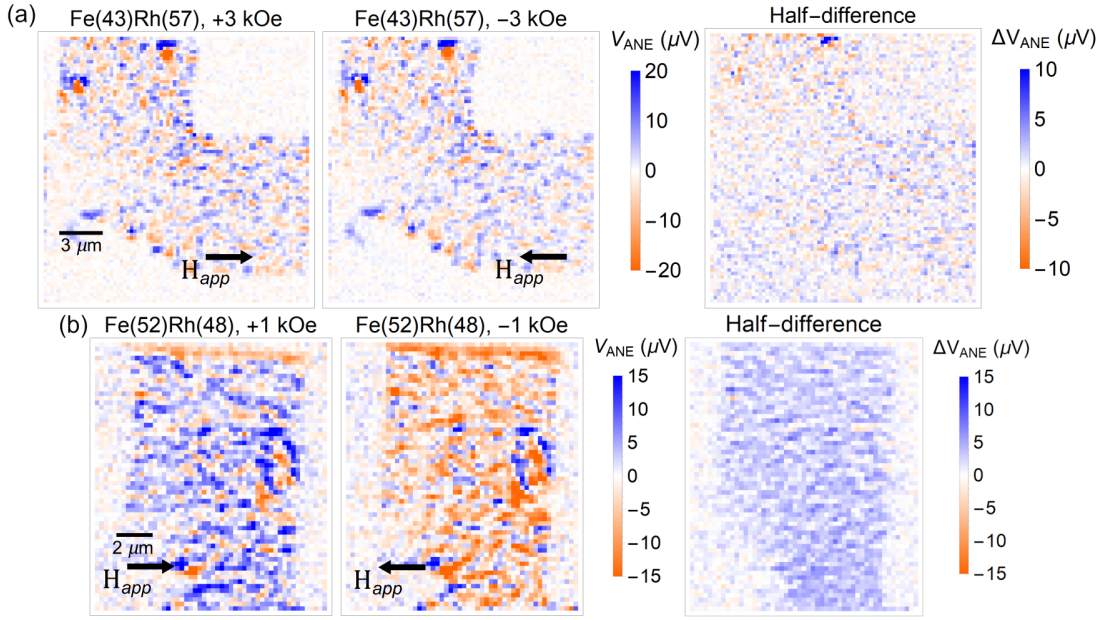

FIG. 11: ANE images of (a) $Fe_{0.43}Rh_{0.57}$ and (b) $Fe_{0.52}Rh_{0.48}$ at 298 K. Taking half-differences between positive and negative field shows unpinned moments in $Fe_{0.52}Rh_{0.48}$ and not in $Fe_{0.43}Rh_{0.57}$. This suggests that the unpinned UMs in $Fe_{0.52}Rh_{0.48}$ and $Fe_{0.47}Rh_{0.53}$/Pt are not due to a residual FM phase near the bottom FeRh/MgO interface, but arise instead from uncompensated excess Fe moments in the bulk.

Both $Fe_{0.43}Rh_{0.57}$ and $Fe_{0.52}Rh_{0.48}$ show submicron regions of positive and negative contrast similar in size, shape, and signal magnitude to the pinned UMs in the $Fe_{0.47}Rh_{0.53}$ samples. This indicates that any contribution from LSSE to the V_{ANE} images of Pt/FeRh is smaller than the contribution from ANE. Interestingly, we observe both pinned and unpinned moments in the $Fe_{0.52}Rh_{0.48}$ sample, shown in the half-difference image, whereas we observe only pinned moments in the $Fe_{0.43}Rh_{0.57}$ sample. The unpinned UMs from uncapped $Fe_{0.52}Rh_{0.48}$ generate V_{ANE} of similar magnitude as the unpinned UMs in $Fe_{0.50}Rh_{0.50}$/Pt, which indicates that the unpinned UMs in $Fe_{0.47}Rh_{0.53}$/Pt are most likely not caused by the Pt capping layer. In addition, our observation of unpinned UMs in $Fe_{0.52}Rh_{0.48}$ and not $Fe_{0.43}Rh_{0.57}$ is inconsistent with both strain and chemical diffusion-induced residual FM near the bottom FeRh/MgO interface, because both of these mechanisms predict more residual FM at higher Rh concentrations[38]. Instead, our results are more consistent with unpinned

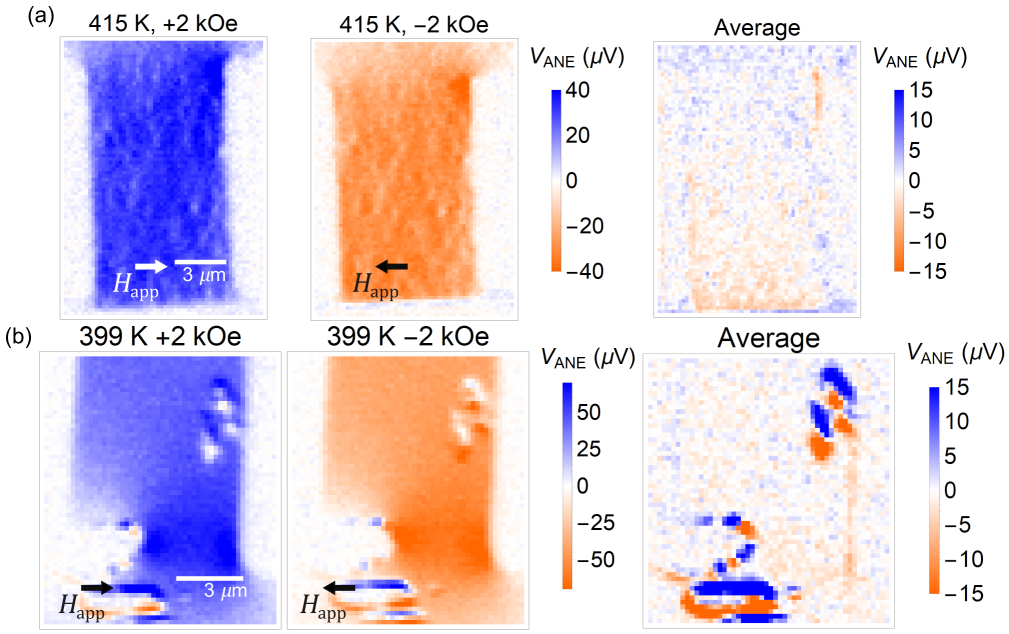

FIG. 12: Imaging the same (a) $Fe_{0.43}Rh_{0.57}$ and (b) $Fe_{0.52}Rh_{0.48}$ with $H_{app} = \pm 2$ kOe along x. Similar to the $Fe_{0.47}Rh_{0.53}$/Pt sample, the lack of contrast in the average image in the FM phase shows that the pinned UMs disappear above T_C (although some dipolar artifacts are visible in (b) due to dirt on the sample surface).

UMs from excess Fe. Because perfect AF ordering of FeRh assumes exactly 50/50 stoichiometry, we expect the excess Fe atoms in the bulk at higher Fe concentration to be uncompensated.

We check that V_{ANE} in Fig. 11 is due to the Néel order and not spatial inhomogeneity in electrical resistance or sample quality by imaging the same devices in the FM phase in Fig. 12. In both $Fe_{0.43}Rh_{0.57}$ and $Fe_{0.52}Rh_{0.48}$, we observe nearly uniform FM and the inhomogeneous contrast in the AF phase disappears, seen by taking the average between images at positive and negative $H_{app} = 2$ kOe. (Particles of dirt on the $Fe_{0.52}Rh_{0.48}$ sample produce non-magnetic dipole-like artifacts from the in-plane charge Seebeck effect.)

Appendix E: Effects of field-cooling on AF domains

Previous reports on 50 nm-thick $Fe_{0.50}Rh_{0.50}$[63,64] showed reorientation of the bulk Néel order by field-cooling, which was measured using the antiferromagnetic anisotropic magnetoresistance (AMR). Pinned UMs in the AF phase are exchange-coupled to the Néel order, therefore if field-cooling reorients the AF domains in our samples we expect to observe

changes in the room-temperature V_{ANE} images. In Fig. 13 we first field-cool the device from Fig. 1 and 2 of the main text with $H_{FC} = 2$ kOe along x, acquire an ANE image, then field-cool with $H_{FC} = 2$ kOe along y and acquire another ANE image. We assume the local T_C to be the temperature at which $R(T)$ starts increasing, as in Fig. 3, and heat 10 K above T_C before field-cooling. Within our resolution and noise level, we observe no changes in the V_{ANE} images after field-cooling, which is shown by the lack of contrast in the half-difference image. This is consistent with our findings in Appendix F that the pinned UM structure near T_C is unaffected by H_{FC}.

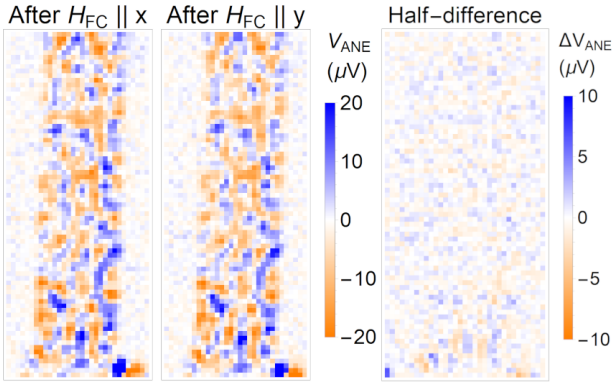

FIG. 13: Imaging the FeRh/Pt sample from Fig. 1 and Fig. 2 of the main text after cooling at $H_{FC} = 2$ kOe, first along x and then along y. The lack of contrast in the half-difference image indicates that we observe no effect of field-cooling on the structure of the AF UMs.

In Fig. 14, we measure antiferromagnetic AMR of another $Fe_{0.47}Rh_{0.53}$/Pt device from the same chip after field-cooling. We again heat 10 K above T_C by Joule heating from DC current, following the procedure of Ref.[63], and measure the longitudinal resistance R using a lock-in amplifier and a Wheatstone bridge. R depends on the average Néel orientation $\vec{N}$ as $R = R_0 + \Delta R_{AMR} \cos^2\theta$, where θ is the angle between $\vec{N}$ and the current density $\vec{j}$. We first measure R at room temperature and $H_{app} = 2$ kOe as a function of in-plane field angle in Fig. 14(a) to measure AMR from any residual FM or uncompensated moments. In Fig. 14(b) we then measure R after repeatedly alternating H_{FC} along x and y, which maximizes ΔR. We observe no ΔR in either case. From our noise level we place an upper bound of $\Delta R/R = 10^{-6}$ on any FM AMR at 298 K and $\Delta R/R = 10^{-5}$ on the maximum AF AMR. For comparison, the two existing studies on AF AMR in FeRh report $\Delta R/R = 1.7 \times 10^{-3}$ and 1.0×10^{-4}, respectively[63,64]. Field-cooling therefore has no effect on the AF domain structure in our 20 nm-thick samples, which may be due to an increased

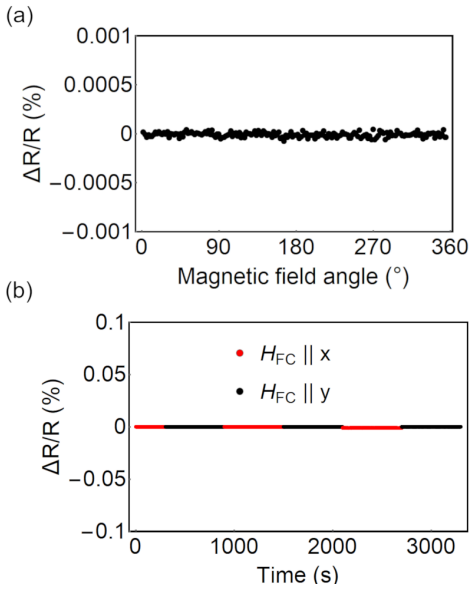

FIG. 14: Measuring the effects of field-cooling on the overall Néel orientation of another FeRh/Pt device using antiferromagnetic AMR. (a) Longitudinal resistance R as a function of in-plane magnetic field angle at $H_{app} = 2$ kOe. (b) Repeated measurements of R while varying the direction of H_{FC} by 90°, which maximizes ΔR from AMR. We observe no ΔR in both cases, which means that both the pinned UMs and the AF domains are unaffected by field-cooling, at least at $H_{FC} = 2$ kOe.

effect of strain in our 20 nm-thick samples than in the 50 nm-thick samples used in the other studies.

Appendix F: Dependence of exchange-biased FM domains on H_{FC}, $Happ$, and f

In this section we investigate the dependence of exchange-biased emergent FM on the applied magnetic field H_{app}, the cooling field H_{FC}, and the laser fluence F. In conventional positive exchange bias in AF/FM multilayers, the orientation of the pinned AF UMs is set by field-cooling. Therefore, we first heat to 10 K above T_C measured with $R(T)$ as before and then field-cool while applying $H_{FC} = +2$ kOe along x before imaging the increasing-temperature branch of the phase transition in Fig. 15(a). We then field-cool at $H_{FC} = -2$ kOe before imaging again in Fig. 15(b). In both sets of images we apply $H_{app} = 100$ Oe along $+x$, because it is larger than the 50 Oe local coercivity field in the FM phase and smaller than the 470 Oe coercivity field of the unpinned UMs in the AF phase.

If the orientation of the pinned UMs is set by H_{FC}, we expect that they would be set along $+x$ in Fig. 15(a) and $-x$ in Fig. 15(b). Assuming an antiferromagnetic exchange coupling

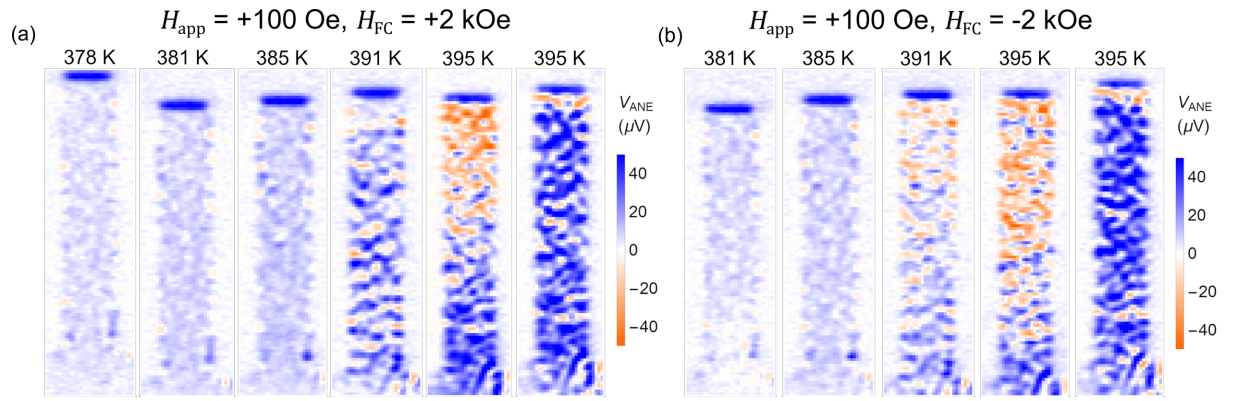

FIG. 15: Dependence of FM domains opposite to H_{app} on the field-cooling field H_{FC}. (a,b) V_{ANE} imaging after field-cooling with $H_{FC} = +2$ kOe (a) and -2 kOe (b) along x to set the orientation of the AF UMs. We observe antiparallel exchange bias in both configurations, which means that H_{FC} does not affect the orientation of the pinned UMs.

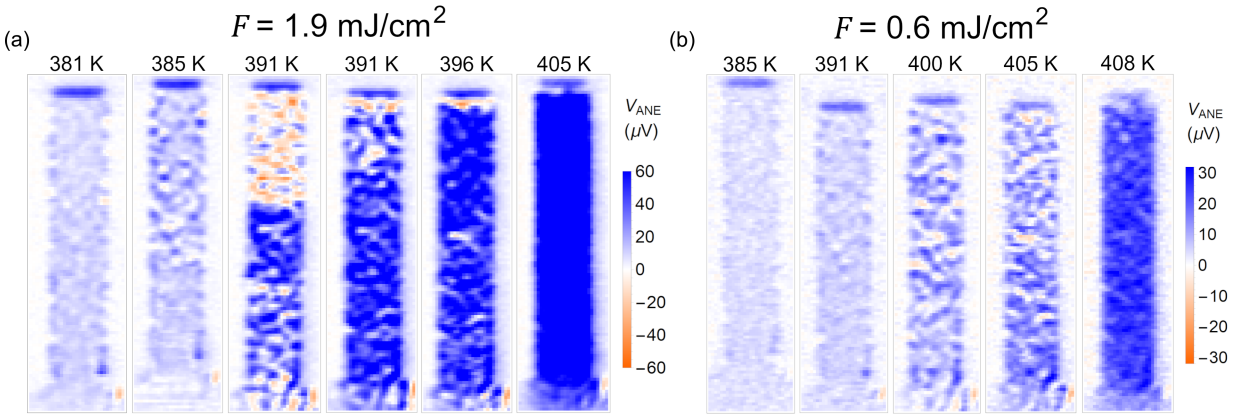

FIG. 16: Phase transition imaging at (a) laser fluence $F = 1.9$ mJ/cm^2 and (b) $F = 0.6$ mJ/cm^2. We observe FM domains opposite H_{app} only at the higher fluence, which indicates that the repeated heating and cooling from the laser pulse train are necessary to induce a metastable frustrated spin state.

J_{F-AF} between emergent FM and pinned UMs, we would therefore expect FM spins pinned opposite to H_{app} only in Fig. 15(a) and not 15(b). Instead, we observe emergent FM spins opposite H_{app} in both cases. This result indicates that the pinned UMs are unaffected by field-cooling at least up to $H_{FC} = 2$ kOe, which is further supported by the lack of any resolvable change in room-temperature V_{ANE} images after field-cooling.

After varying H_{FC}, we image the phase transition at laser fluence $F = 1.9$ mJ/cm^2 in Fig. 16(a), and then at 0.6 mJ/cm^2 in Fig. 16(b). Both images are taken with $H_{FC} = +2$ kOe and $H_{app} = +2$ kOe along x. From the determination of laser heating in Appendix G, we estimate the peak temperature increase at these fluences to be 10 K and 3 K, respectively.

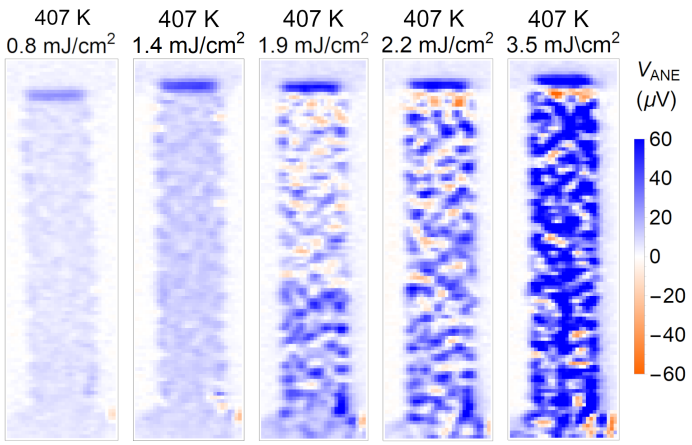

FIG. 17: Imaging the vertical branch of a Hall cross at fixed $T = 407$ K and $H_{app} = 2$ kOe as a function of laser fluence f. We observe exchange bias only at the intermediate fluences $F = 1.9$ mJ/cm^2 and 2.2 mJ/cm^2. At lower fluences, the peak temperature increase is not high enough to unpin the pinned UMs. At higher fluence, the laser locally heats into the FM phase, which remains stable after cooling due to phase transition hysteresis.

We do not observe antiparallel exchange bias at the lower fluence, which suggests that the pulsed laser has a different effect on the magnetic structure than the resistive heater we employ to adiabatically heat the whole sample. Imaging at fixed temperature as a function of fluence in the vertical branch of a cross in Fig. 17 shows FM domains opposite H_{app} for intermediate fluences between 1.4 mJ/cm^2 and 3.5 mJ/cm^2. Higher fluences locally heat the FeRh into the FM phase, which persists after cooling because of the hysteresis of the 1st-order phase transition. This means that in the exchange biased-state the sample locally remains in a mixed phase of AF and FM. Imaging the horizontal branch of a similar cross at 402 K in Fig. 18 shows similar behavior: we observe FM domains perpendicular to H_{app} above 1.4 mJ/cm^2, and the FM domains disappear in the FM phase. We speculate that repeated heating and cooling from the pulsed laser cause the UMs to unpin and undergo repeated reversals before becoming pinned in different directions. After the UMs become repinned, they rotate the FM spins to form domains in many different orientations in-plane.

Appendix G: Laser-induced heating in FeRh/Pt

In this section we determine the laser-induced temperature profile $T(r, z, t)$ in FeRh/Pt as a function of fluence. Because we employ a picosecond pulsed laser and detect V_{ANE}

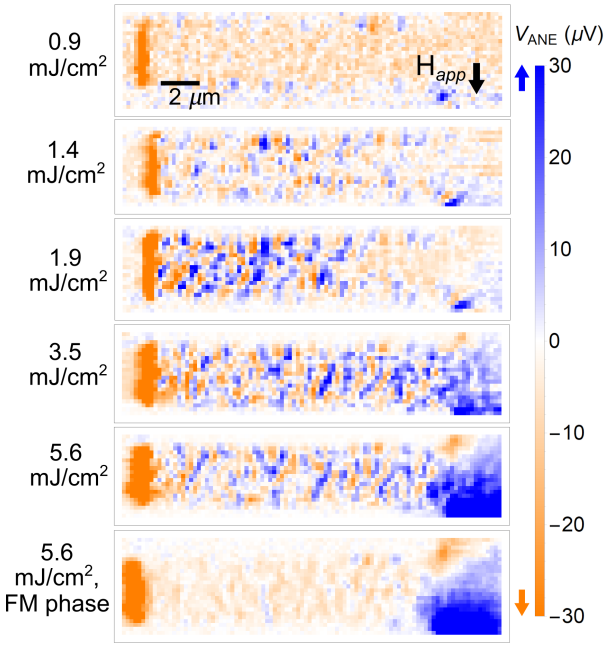

FIG. 18: Fluence dependence of the horizontal branch of a similar Hall cross as in Fig. 17 at fixed 402 K and $H_{app} = 2$ kOe. We observe FM domains perpendicular to H_{app} for fluences between 1.9 mJ/cm^2 and 5.6 mJ/cm^2. After driving into the full FM phase by heating and cooling, the FM domains perpendicular to H_{app} disappear.

using a homodyne mixing circuit and a lock-in amplifier, directly measuring $T(r, z, t)$ is difficult. We therefore follow a procedure detailed in our previous work[26,27,30]: we first simulate $T(r, z, t)$ using finite-element methods. Because the absorption depths of the Pt and FeRh layers are comparable to the layer thicknesses, causing a complicated series of internal reflections, the overall fraction of light absorbed is not well-known *a priori*. We account for this uncertainty by assuming that the simulated $\Delta T(r, z, t)$ is accurate up to an unknown overall scaling factor. We experiementally determine this factor by converting $\Delta T(r, z, t)$ into a transient resistance change $\Delta R(t)$ for a given DC current I_{DC}, computing the resulting lock-in voltage $V_{LI}(I_{DC})$, then scaling ΔT to match experimental measurements of $V_{LI}(I_{DC})$ in an FeRh/Pt device. Here we present the scaled simulation results; details of the scaling procedure, including the calibration of the collection circuit transfer coefficient, can be found in Refs.[26] and [30].

We perform finite-element simulations of laser heating using the COMSOL Multiphysics® software package. We numerically solve the radially symmetric heat equation, modeling the laser as a distributed heat source that exponentially decays with depth. We employ absorption coefficients of 80 μm^{-1} and 2.4×10^3 μm^{-1} at 785 nm wavelength for Pt and

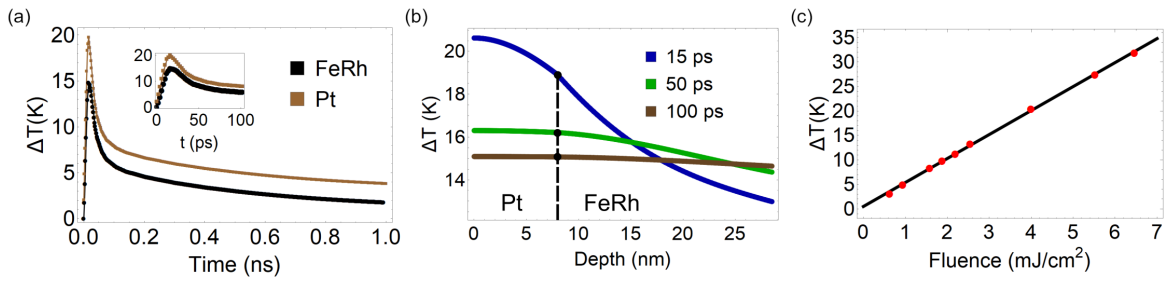

FIG. 19: Laser-induced temperature profile in FeRh/Pt. (a) Temperature change $\Delta T(t)$ at the Pt and FeRh layers at the beam center ($r = 0$) at 3 mJ/cm^2 laser fluence. (b) Temperature depth profile $\Delta T(z)$ at $r = 0$ at 15 ps, 50 ps, and 100 ps after the pulse arrival. (c) Peak ΔT at $r = 0$ in the center of the FeRh thickness as a function of laser fluence f.

FeRh, taken from Refs. [65] and [66], respectively. We assume 8 nm-thick Pt and 20 nm-thick FeRh at a base temperature of 293 K.

In Fig. 19(a) we plot the temperature increase $\Delta T(t)$ at the center of the beam ($r = 0$) in the center of both the Pt and FeRh layers for $f = 3.0$ mJ/cm^2 fluence as used in the main text. We find a peak temperature increase of 20 K and 15 K for the Pt and FeRh layers, respectively. In Fig. 19(b) we plot $\Delta T(z)$ at $r = 0$ at peak heating – 15 ps after the beam arrival – as well as subsequent 50 ps and 100 ps times. Finally, in Fig. 19(c) we plot the maximum ΔT in the midpoint of the FeRh layer at $r = 0$ as a function of fluence f. The minimum fluence at which we find exchange-biased FM domains near T_C is 1.9 mJ/cm^2, which heats the FeRh by 10 K.